JASA ARTICLE

Ultrasound characterization of bioinspired functionally graded soft-to-hard composites: Experiment and modeling

Ali Aghaei,[1,a)] Nicolas Bochud,[1,b)] Giuseppe Rosi,[1,c)] Quentin Grossman,[2] Davide Ruffoni,[2,d)] and Salah Naili[1,e)]
[1]*Univ Paris Est Creteil, Univ Gustave Eiffel, CNRS, UMR 8208, MSME, F-94010 Créteil, France*
[2]*Mechanics of Biological and Bioinspired Materials Laboratory, Department of Aerospace and Mechanical Engineering, University of Liège, Quartier Polytech 1, Allée de la Découverte 9, B-4000 Liège, Belgium*

ABSTRACT:
Functional grading is a distinctive feature adopted by nature to improve the transition between tissues that present a strong mismatch in mechanical properties, a relevant example being the tendon-to-bone attachment. Recent progress in multi-material additive manufacturing now allows for the design and fabrication of bioinspired functionally graded soft-to-hard composites. Nevertheless, this emerging technology depends on several design variables, including both material and mechanistic ingredients, that are likely to affect the mechanical performance of such composites. In this paper, a model-based approach is developed to describe the interaction of ultrasound waves with homogeneous and heterogeneous additively manufactured samples, which respectively display a variation either of the material ingredients (e.g., ratio of the elementary constituents) or of their spatial arrangement (e.g., functional gradients, damage). Measurements are performed using longitudinal bulk waves, which are launched and detected using a linear transducer array. First, model is calibrated by exploiting the signals measured on the homogeneous samples, which allow identifying relationships between the model parameters and the material composition. Second, the model is validated by comparing the signals measured on the heterogeneous samples with those predicted numerically. Overall, the reported results pave the way for characterizing and optimizing multi-material systems that display complex bioinspired features. © *2022 Acoustical Society of America*. https://doi.org/10.1121/10.0009630

(Received 6 October 2021; revised 13 January 2022; accepted 4 February 2022; published online 4 March 2022)
[Editor: Michael R Haberman] Pages: 1490–12

I. INTRODUCTION

Joining soft-to-hard materials is a frequent requirement in modern engineering applications (e.g., aerospace and tissue engineering) that rises to several challenges. Such attachment generally needs to effectively transfer mechanical stresses and sustain large forces for several millions of loading cycles without being damaged. To this end, different strategies can be found in nature to alleviate stress concentrations at the interface between materials with highly dissimilar properties, one of them being the use of functionally graded interphases (Dunlop *et al.*, 2011).

In this context, the development of bioinspired composite materials has been limited for many years by the ability of traditional manufacturing methods to synthesize and assemble materials with different properties. However, recent progress in additive manufacturing [also known as three-dimensional (3D) printing] has unlocked this technical burden and opened new ways to design and fabricate materials with dissimilar properties (Velasco-Hogan *et al.*, 2018). In particular, material jetting is considered as a powerful process for multi-material additive manufacturing. Similar to biological systems engineered by nature through a bottom-up approach, this technique arranges dissimilar building blocks at several length scales to build a final component with enhanced and adaptable mechanical performance (Rafiee *et al.*, 2020; Studart, 2016). Thanks to its high resolution (i.e., voxels with side lengths around 40 μm) and the possibility to locally tailor the material composition, numerous studies used this strategy to prototype bioinspired heterogeneous structures (Jia *et al.*, 2019; Libonati *et al.*, 2016; Zorzetto and Ruffoni, 2019), in particular functionally graded soft-to-hard composites (Liu *et al.*, 2017; Mirzaali *et al.*, 2020a; Perikamana *et al.*, 2018). The latter are typically designed as multilayers whose material properties smoothly evolve along one or two dimensions, overall resulting in materials with superior behavior and manifold functionalities.

However, to fully exploit the potential of these emerging composites, there is an unmet need in developing methods for characterizing the quality of the printing process and the mechanics of the manufactured samples. Indeed, multi-material jetting typically depends upon several characteristics, such as the properties of the elementary constituents, their spatial arrangement, as well as the printing orientation and resolution, but their impact on the overall mechanical performance is still elusive. Several characterization techniques have been applied recently, including tensile testing

[a)]ORCID: 0000-0001-8488-8745.
[b)]Electronic mail: nicolas.bochud@u-pec.fr, ORCID: 0000-0002-2136-1353.
[c)]ORCID: 0000-0001-7699-7300.
[d)]ORCID: 0000-0003-3714-7594.
[e)]ORCID: 0000-0001-7153-0840.

 0001-4966/2022/151(3)/1490/12/$30.00

https://doi.org/10.1121/10.0009630

(Mirzaali *et al.*, 2020a; Slesarenko and Rudykh, 2018), dynamic mechanical analysis (Meisel *et al.*, 2018; Zorzetto *et al.*, 2020), and ultrasonic testing (Honarvar and Varvani-Farahani, 2020), altogether providing guidelines for process modifications and subsequent design optimization. Among these, quantitative ultrasound is thought of as a particularly relevant nondestructive means to probe the quality of functionally graded soft-to-hard composites, because it relies on the use of mechanical waves and thus possesses intrinsic sensitivity to their mechanical properties. Moreover, ultrasound requires limited sample preparation and offers a very fast inspection capability.

Although several researchers proposed the use of ultrasound-based methods either for the characterization of monolithic and graded materials (Foster *et al.*, 2013; Javidrad and Salemi, 2020; Rubio *et al.*, 2012) or for the detection of defects such as pores, cracks, and microstructural anomalies (Slotwinski *et al.*, 2014), most attention has been given to metal-based additively manufactured products so far. Notwithstanding, a few studies have explored its use for assessing the acoustic and mechanical properties of multi-material inkjet-based products, which are becoming more widespread for the rapid production of models for preoperative planning (e.g., medical implants, tissue-mimicking phantoms) and of passive components for medical devices (Giannatsis and Dedoussis, 2009). For instance, an ultrasound through-transmission method was proposed to quantify the level of anisotropy induced by the printing process, although the polymeric constituent was initially isotropic (Livings *et al.*, 2015). The phase velocity and attenuation characteristics could be determined along different directions, thereby providing a basis for flaw detection. Using a pulse-echo ultrasound technique, Jacquet *et al.* (2015) measured the phase velocity and attenuation of two different materials (i.e., a wax-like support material and a rigid glassy polymer), which were subsequently exploited to design, print, and image multi-material phantoms including heterogeneities with arbitrary geometries. In another related study, Fariñas *et al.* (2016) printed multi-material samples by varying the ratio between the two deposited constituents (i.e., a rigid glassy polymer and an elastomeric polymer) and subsequently measured their acoustic impedances as a function of the mass density using a non-contact ultrasound technique. These earlier studies provided a valuable insight on the acoustic properties of additively manufactured samples. However, to the authors' best knowledge, these were limited to the study of macroscopically homogeneous samples lacking mechanistic ingredients, such as the spatial arrangement of the elementary constituents.

This study therefore aims at understanding the interactions of ultrasound waves with additively manufactured multi-material samples, featuring functional grading and programmed damage. Towards this goal, two sets of samples are fabricated using a polyjet 3D printing technology. The first set consists of macroscopically homogeneous samples obtained by varying the ratio of the two elementary constituents, whereas the second set consists of functionally graded soft-to-hard samples. The adopted biomimetic strategy to design heterogeneous structures is based on the graded tissue system at the tendon-to-bone interphase, which fulfills the challenging task of integrating soft-to-hard tissues over a submillimeter-wide region (Tits and Ruffoni, 2020). A pulse-echo technique using a multielement probe in the MHz-regime is employed to characterize the samples. From the measurements performed on the homogeneous samples, we first identify relationships between the mechanical properties and the material composition by solving a model-based inverse problem. In a second part, these relationships are used to feed a wave propagation model that accounts for the structural and material complexity of the functionally graded samples. Overall, our modeling results show an excellent agreement with the measured signals for cases where the transition region is on the order of magnitude of the bulk wavelength, thereby providing a nondestructive means for characterizing and optimizing bioinspired multi-material composites.

The remainder of the paper is organized as follows: Sec. II presents the methods used to additively manufactured the samples and to perform the ultrasound measurements. Section III introduces the theoretical fundamentals of our modeling approach, which relies on the Szabo wave equation and the transfer matrix formalism. The model calibration and validation results are then exposed in Secs. IV–V. Finally, the strengths and limitations of the proposed approach are discussed in Sec. VI.

II. SAMPLES AND ULTRASOUND MEASUREMENTS

Multi-material additive manufacturing of the samples was achieved using a commercial polyjet 3D printer (Objet 260, Stratasys), which applies a layer-by-layer method where multiple streams of UV-curable photopolymers are jetted through printing nozzles onto a building tray (Zorzetto *et al.*, 2020). At the microscale (voxel level), custom-made patterns can be obtained by spreading two photopolymers with highly dissimilar properties, i.e., a rigid glassy polymer (commercial name VeroWhitePlus, VW^+) and an elastomeric polymer (commercial name TangoBlackPlus, TB^+), on a chessboard-like volume as depicted in Fig. 1. From a macroscopic viewpoint, this process allows printing both homogeneous samples with any intermediate volume fraction [see Fig. 1(a)] and heterogeneous samples with a functional grading between the soft and hard photopolymers [see Fig. 1(b)].

Two sets of 3D-printed samples were investigated here. The first set consisted of 11 homogeneous plate-like samples displaying different volume fractions of the compliant photopolymer (TB^+), denoted by V_f of TB^+, which ranged from 0 to 100% with a step of 10%. Their overall dimensions were $20 \times 16 \times 4$ mm^3, printed using random dithering patterns along the x, y, and z directions, respectively. The second set consisted of six heterogeneous samples, which were all compound of a soft layer (i.e., TB^+), a hard layer (i.e., VW^+), and an interphase in-between, which was inspired by

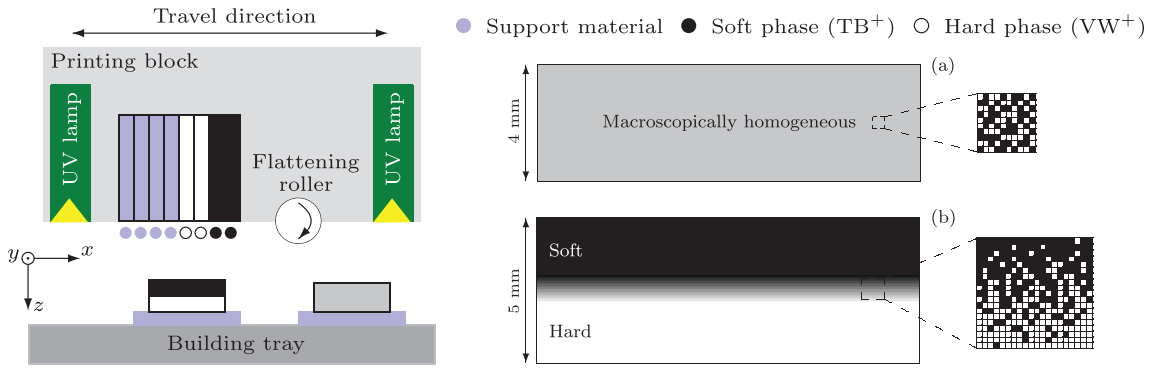

FIG. 1. (Color online) Schematic representation of the polyjet 3D printing process, which allows for the additive manufacturing of both (a) homogeneous samples (e.g., $V_f = 50\%$) and (b) heterogeneous samples with functional grading, obtained by locally spreading two photopolymers with highly dissimilar properties.

the tendon-to-bone attachment. For the latter, different profiles have been selected for the interphase layer by adjusting the relative proportions of the two photopolymers along the z-direction (see Fig. 2). This printing direction was chosen to minimize photopolymer diffusion and mixing between different layers (Zorzetto *et al.*, 2020). The first sample was a bilayer that displays a sharp transition between the soft and hard layers, whose thickness amounts to 2.2 mm and 2.8 mm, respectively [Fig. 2(a)]. Likewise, the second sample was a trilayer with a 2 mm-thick soft layer, a 2.232 mm-thick hard layer, and a 768 μm-thick homogeneous interphase in-between [Fig. 2(b)]. Apart from these two profiles that served us as a reference, two further profiles highlighting functional grading have been printed, one with a linearly varying interphase layer [see Fig. 2(c)], the other with a smoothly varying interphase layer [see Fig. 2(d)]. It should be noted that these bioinspired profiles were designed based on recent multiscale modeling results (Aghaei *et al.*, 2021; Liu *et al.*, 2014), which showed that the native tendon-to-bone attachment can be seen as a continuous functionally graded material. Moreover, to mimic local damage characteristics such as tears and fissures, which are acknowledged to be footprint of clinical burden related to physical overloading or pathology (Benjamin *et al.*, 2007; Deymier *et al.*, 2019), slightly modified versions of these two functionally graded profiles were designed too [see Figs. 2(e)–2(f)]. Programmed damage was achieved by assigning a sudden and local variation of the volume fraction to a finite-width layer, i.e., 64 μm wide, across the interphase. The overall dimensions of the six heterogeneous samples were $20 \times 16 \times 5$ mm^3, printed with a voxel size of $120 \times 120 \times 32$ μm^3 along the x, y, and z directions, respectively. The thickness of the interphase (i.e., 768 μm) was chosen according to physiological observations found in the literature (Saadat *et al.*, 2016), which showed that the size of the tendon-to-bone attachment typically ranges from a few hundred micrometers to some millimeters depending on the insertion site. Besides, the dimensions of the two surrounding layers were chosen based on a trade-off between temporal resolution and attenuation of the recorded signals, according to the ultrasound characteristics of the probe. Tables summarizing the dimensions and specificities of the two sets of 3D-printed samples are included as supplementary material.[1]

A pulse-echo configuration was considered in this work, where longitudinal bulk waves were launched normally through the samples along the z-direction (see Fig. 3). The employed device consisted of a multielement probe (Imasonic, SAS, France), which was driven by a programmable multi-channel electronics (Advanced OEM Solutions, West Chester, USA). This type of device, initially dedicated to medical imaging, has recently also been used for the mechanical characterization of materials, particularly for monitoring the health status of aeronautical structures (Leleux *et al.*, 2013) or for reconstructing the anisotropic elastic tensor of plate-like samples (Bochud *et al.*, 2018).

The measurements were carried out in a water tank by using a linear transducer array that consisted of 32 elements. Each element had a width of 0.5 mm and a height of 12 mm, resulting in a total emission surface of 16×12 mm^2. The transducer array operated at a central frequency $f_c = 2.25$ MHz (-6 dB power spectrum spanning a frequency range from 1.5 to 3 MHz) and the array pitch was 0.5 mm. This probe was used to transmit a wideband plane wave by concurrently firing a pulse on all emitters. The received signals, which were digitized at a sampling rate of 100 MHz and quantized with a 12-bit resolution, were recorded during 20 μs. The advantage of using a linear transducer array in plane wave mode was twofold. First, because the bulk wavelength was small compared to the total width of the transducer array, beam diffraction effects were negligible and could be neglected in the subsequent processing and modeling of the received signals. Second, it allowed averaging the received signals across all the elements of the probe to enhance the signal-to-noise ratio of the measurement. All measurements were performed under controlled water temperature (20 °C). For the measurement of the heterogeneous samples, it should be noted that the soft layer was always directed towards the transducer array (as in Fig. 3).

III. MECHANICAL MODELING

The wave interactions with the functionally graded samples (recall Fig. 2) can be approximated by a model

https://doi.org/10.1121/10.0009630

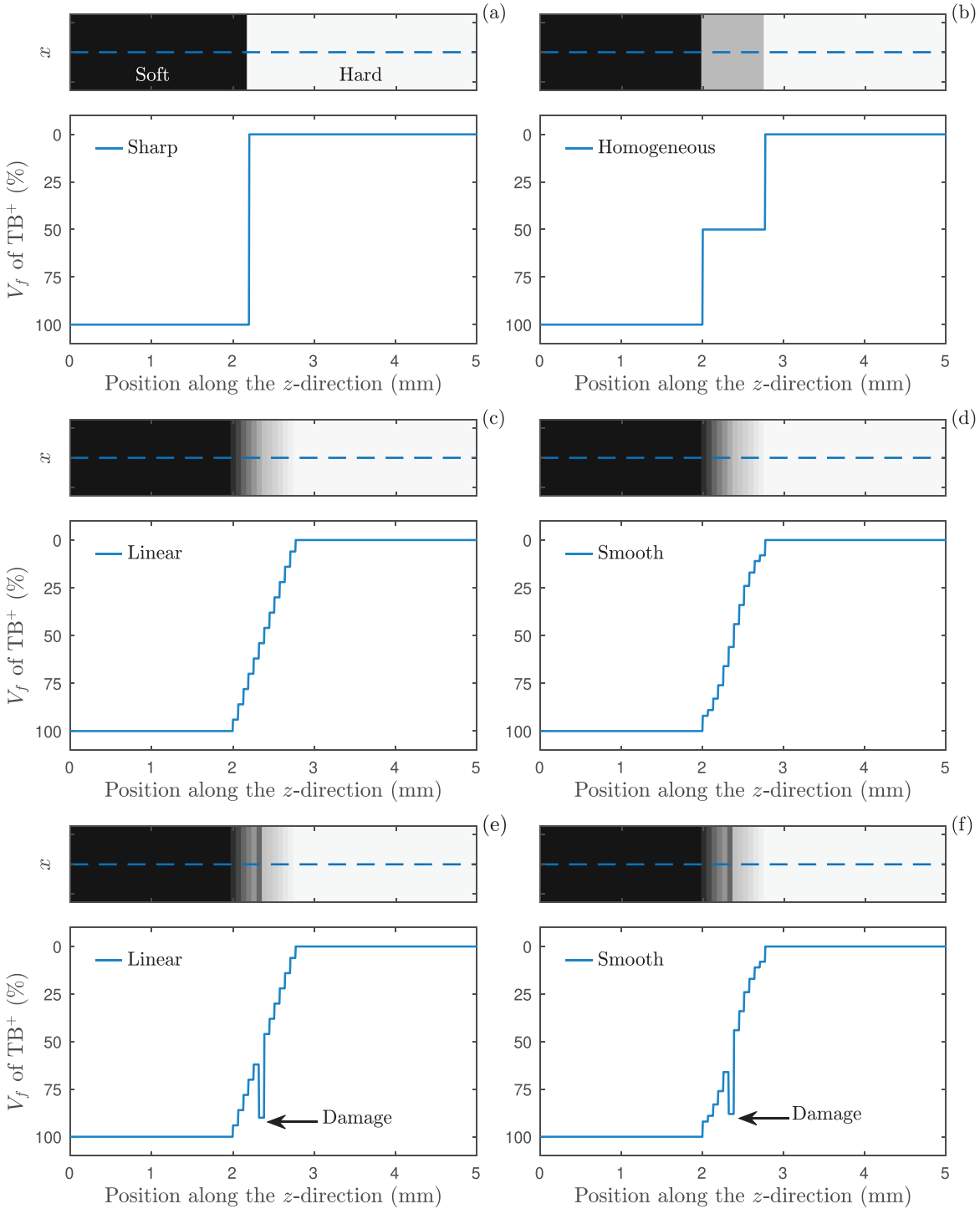

FIG. 2. (Color online) Overview of the spatial arrangement of the volume fractions for the six heterogeneous samples: (a) Bilayer sample with a sharp transition, (b) trilayer sample with a homogeneous interphase, (c) sample with a linearly varying interphase, (d) sample with a smoothly varying interphase, (e) sample with a localized damage across the linearly varying interphase, and (f) sample with a localized damage across the smoothly varying interphase. For each subplot, the upper panel represents a view of the sample in the x–z plane, where the dashed blue line makes reference to the spatial arrangement of the volume fraction V_f of TB$^+$ along the z-direction depicted in the lower panel (continuous blue line).

based on the transfer matrix formalism (Bochud *et al.*, 2015). This formalism was here adapted to describe the wave propagation in a finite multilayered viscoelastic medium exhibiting a power-law attenuation. Several observations guided the choice of this model. First, in the frequency bandwidth of interest, the wavelengths of the longitudinal bulk wave, ranging from around 500 μm to 2.5 mm, were much larger than the typical size of the heterogeneities (i.e., voxel size of 32 μm along the z-direction). The functionally graded samples can thus be considered as successive piecewise homogeneous media. Second, since the viscous behavior of the photopolymers exhibited

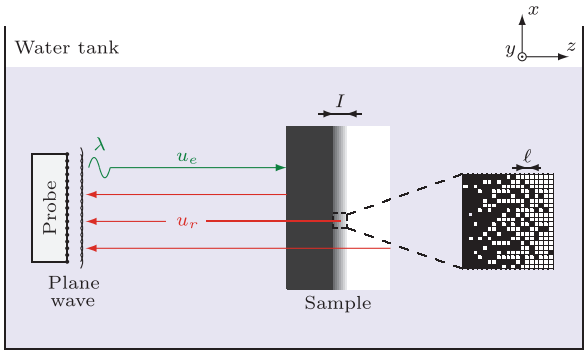

FIG. 3. (Color online) Schematic representation of the pulse-echo configuration used to record the ultrasound measurements. The emitted signal, u_e (in green), is a plane longitudinal wave, whereas the recorded signal, u_r (in red), is compound of the reflections from the front and back faces of the sample, plus that interacting with the interphase. The bulk wavelength λ is on the order of magnitude of the interphase thickness I and much larger than the typical size ℓ of the heterogeneities, i.e., $\lambda \sim I \gg \ell$.

dispersive losses that cannot be accurately described by a rheological Voigt model (whose attenuation is proportional to the square of the angular frequency ω^2), we sought for a model that allowed describing more complex attenuation mechanisms (e.g., relaxation phenomena). This can be achieved by means of the Szabo wave equation (Szabo and Wu, 2000), which approximates power-law media with an attenuation in the form

$$\alpha(\omega) = \alpha_0 \omega^r, \tag{1}$$

where α_0 is a constant and the dimensionless exponent r typically ranges between 1 and 2 for materials belonging to the class of polymers and to some biomaterials (Raišutis *et al.*, 2007; Sasso *et al.*, 2007).

A. Szabo wave equation

Formally, the model introduced by Szabo and Wu (2000) allowed such modeling approach to be generalized to cases for which $r \neq 2$, by introducing a fractional derivative in the wave equation as

$$\frac{\partial^2 u(z,t)}{\partial z^2} - \frac{1}{v_0^2}\frac{\partial^2 u(z,t)}{\partial t^2} - \frac{2\alpha_0}{v_0 \cos\left(\frac{\pi}{2}r\right)}\frac{\partial^{r+1} u(z,t)}{\partial t^{r+1}} = 0, \tag{2}$$

where t is the time, v_0 is a constant, and the third term accounts for dispersive losses. By assuming a general harmonic solution for the displacement in the z-direction, $u(z,t) = \exp(j(\omega t - kz))$, which satisfies the power-law Eq. (2), it can be shown that the dispersion relation between the complex wavenumber $k(\omega)$ and the angular frequency ω can be written as

$$k(\omega) = \sqrt{\frac{\omega^2}{v_0^2} - (j\omega)^{r+1}\frac{2\alpha_0}{v_0 \cos\left(\frac{\pi}{2}r\right)}}, \tag{3}$$

where j is the unit imaginary number. Note that Eq. (3) is valid for all $r \neq 1$. Under the hypothesis of small wavelength $\lambda = 2\pi/k(\omega)$ and low attenuation α_0, i.e., $\lambda\alpha_0 \ll 1$, the dispersion relation [Eq. (3)] can be simplified according to Kelly *et al.* (2008),

$$k(\omega) = \frac{\omega}{v_0} - j\frac{\alpha_0 (j\omega)^r}{\cos\left(\frac{\pi}{2}r\right)}. \tag{4}$$

By invoking the de Moivre's identity for $\pi/2$, i.e., $j^r = \cos(\pi r/2) + j\sin(\pi r/2)$, the imaginary part of Eq. (4) leads to the power-law attenuation given by Eq. (1), whereas the real part allows expressing the phase velocity as

$$v(\omega) = \frac{\omega}{\Re(k(\omega))} = \left(\frac{1}{v_0} + \alpha_0 \tan\left(\frac{\pi}{2}r\right)\omega^{r-1}\right)^{-1}, \tag{5}$$

where $\Re(\cdot)$ designates the real part of the quantity. Alternatively, Eq. (5) can be written as

$$v(\omega) = \left(\frac{1}{v_1} + \alpha_0 \tan\left(\frac{\pi}{2}r\right)(\omega^{r-1} - 1)\right)^{-1}, \tag{6}$$

where v_1 is the phase velocity at a reference frequency $\omega_0 = 1$ Hz. Since Eq. (6) presents a singularity when r is an odd integer number (e.g., $r = 1$), another expression for the phase velocity can be derived in this particular case (Kelly *et al.*, 2008; Szabo and Wu, 2000),

$$v(\omega) = \left(\frac{1}{v_1} - \frac{2\alpha_0}{\pi}\omega^{r-1}\ln(\omega)\right)^{-1}, \tag{7}$$

where $\ln(\cdot)$ designates the natural logarithm of the quantity. Combining Eqs. (1) and (7) yields a dispersion relationship for $r = 1$ as

$$k(\omega) = -j\alpha_0\omega + \frac{\omega}{v_1} - \frac{2\alpha_0}{\pi}\omega\ln(\omega). \tag{8}$$

B. Transfer matrix formalism for a power-law medium

Let us consider a finite multilayered system consisting of $M+1$ homogeneous layers with the same cross-sections, as shown in Fig. 4.

Note that in this system, layer 1 represents the water path between the probe and the investigated sample, whereas layer $M+1$ is considered as a semi-infinite water layer. A general harmonic solution to the Szabo wave Eq. (2) can be stated in the frequency-domain for each layer i, with $i = 1, \ldots, M$, as

$$\begin{aligned} u_i(z,\omega) &= u_i^f(z,\omega) + u_i^b(z,\omega) \\ &= A_i \exp(-jk_i(\omega)z) + B_i \exp(jk_i(\omega)z), \end{aligned} \tag{9}$$

where $u_i^f(z,\omega)$ and $u_i^b(z,\omega)$ stand for the forward- and backward-propagating components of the displacement in

https://doi.org/10.1121/10.0009630

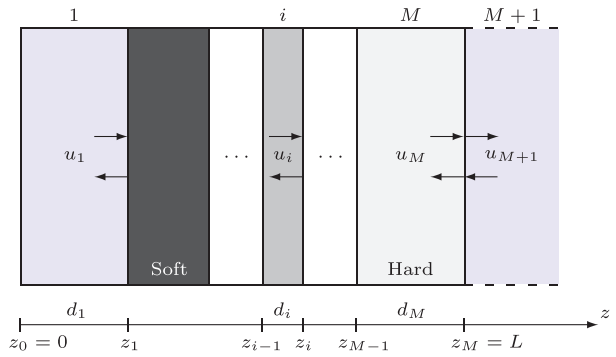

FIG. 4. (Color online) Schematic of the finite multilayered system used to model the wave interactions with the functionally graded soft-to-hard samples immersed in a water tank (in blue).

each layer i, respectively. The complex wavenumber $k_i(\omega)$ of layer i is defined according to Eq. (4) for $r \neq 1$ and Eq. (8) for $r = 1$. In the case of a perfectly bonded interface between two layers, the transmission conditions imply the continuity of displacement and stress across this interface. Expressing these conditions at an arbitrary interface position $z = z_i$ allows characterizing the transition from layer i to layer $i+1$ as in Cretu and Nita (2004),

$$\boldsymbol{u}_{i+1}(z_i,\omega) = \boldsymbol{D}_i(\omega)\boldsymbol{u}_i(z_i,\omega) \quad (i = 1,\ldots,M), \tag{10}$$

where $\boldsymbol{u}_i(z,\omega) = [u_i^f(z,\omega)\, u_i^b(z,\omega)]^T$ is the state vector of layer i, with T being the transpose operator, and $\boldsymbol{D}_i(\omega)$ is the discontinuity matrix, which is defined as

$$\boldsymbol{D}_i(\omega) = \frac{1}{2}\begin{pmatrix} 1+\dfrac{Z_i(\omega)}{Z_{i+1}(\omega)} & 1-\dfrac{Z_i(\omega)}{Z_{i+1}(\omega)} \\ 1-\dfrac{Z_i(\omega)}{Z_{i+1}(\omega)} & 1+\dfrac{Z_i(\omega)}{Z_{i+1}(\omega)} \end{pmatrix}. \tag{11}$$

It should be noted that this matrix only depends on the complex acoustic impedance of the two layers being in contact, which is defined by $Z_i(\omega) = \rho_i\omega/k_i(\omega)$, where ρ_i is the mass density of layer i. In the same way, by considering a harmonic wave propagating in the same homogeneous layer i from position $z = z_{i-1}$ to position $z = z_i$, its transformed displacement can be expressed by means of the propagation matrix $\boldsymbol{P}_i(\omega)$ as

$$\boldsymbol{u}_i(z_i,\omega) = \boldsymbol{P}_i(\omega)\boldsymbol{u}_i(z_{i-1},\omega) \quad (i = 1,\ldots,M), \tag{12}$$

with

$$\boldsymbol{P}_i(\omega) = \begin{pmatrix} \exp\left(-jk_i(\omega)d_i\right) & 0 \\ 0 & \exp\left(jk_i(\omega)d_i\right) \end{pmatrix}, \tag{13}$$

where $d_i = z_i - z_{i-1}$ is the thickness of layer i. The relation between the input and output state vectors for layer i can therefore be expressed as

$$\boldsymbol{u}_{i+1}(z_i,\omega) = \boldsymbol{T}_i(\omega)\boldsymbol{u}_i(z_{i-1},\omega) \quad (i = 1,\ldots,M), \tag{14}$$

where $\boldsymbol{T}_i(\omega) = \boldsymbol{D}_i(\omega)\boldsymbol{P}_i(\omega)$ is the transfer matrix of layer i. The total transfer matrix $\boldsymbol{T}(\omega)$, which describes the overall reflections, transmissions, and losses of the wave propagating across the graded structure from Fig. 4, can then be obtained as the product of transfer matrices from successive layers,

$$\boldsymbol{T}(\omega) = \prod_{i=0}^{M-1} \boldsymbol{T}_{M-i}(\omega), \tag{15}$$

which leads to a relation between the input and output state vectors as

$$\boldsymbol{u}_{M+1}(L,\omega) = \boldsymbol{T}(\omega)\boldsymbol{u}_1(0,\omega). \tag{16}$$

Applying the radiation energy condition at position $z = L$, i.e., $u_{M+1}^b(L,\omega) = 0$, allows solving Eq. (16) for a pulse-echo configuration and thus determining the backward propagating displacement as a function of the imposed displacement at the transmitter location as

$$u_1^b(0,\omega) = -\frac{T_{21}(\omega)}{T_{22}(\omega)}u_1^f(0,\omega), \tag{17}$$

where $T_{2m}(\omega)$, with $m = 1, 2$, denotes the components of the second row of the total transfer matrix $\boldsymbol{T}(\omega)$. It should be noted that $u_1^f(0,\omega)$ is the Fourier transform of the emitted signal $u_e(t)$, which can in practice be measured by taking a delayed version of the signal reflected by a perfect reflector. In the same way, the reflected signal $u_r(t)$ can be retrieved in the time-domain by calculating the inverse Fourier transform of $u_1^b(0,\omega)$. To solve Eq. (17) for the functionally graded samples (recall Fig. 2), it is therefore necessary to have a precise knowledge of the mechanical properties associated with each layer i, namely, ρ, v_1, α_0, and r (if $r \neq 1$). Towards this goal, a model calibration strategy is proposed in Sec. IV.

IV. MODEL CALIBRATION

The set of homogeneous samples was first characterized to derive volume fraction-dependent mechanical properties, which will in turn be used to feed the mechanical model developed to predict the measurements obtained on the heterogeneous samples.

A. Ultrasound characterization of homogeneous samples

To extract ultrasound characteristics, e.g., the phase velocity $v(\omega)$ and attenuation $\alpha(\omega)$, from the measurements performed on the homogeneous samples, a dedicated signal processing approach has been developed. To serve as an example, Fig. 5(a) depicts the raw spatiotemporal signals measured on the stiffest homogeneous sample (i.e., volume fraction V_f of TB^+ equal to 0%), which contain plane wavefronts along with spurious signals due to edge effects. A first step therefore consisted in filtering these edge effects that could cause aliasing, in order to retain only the plane wavefronts for the posterior determination of the amplitude and

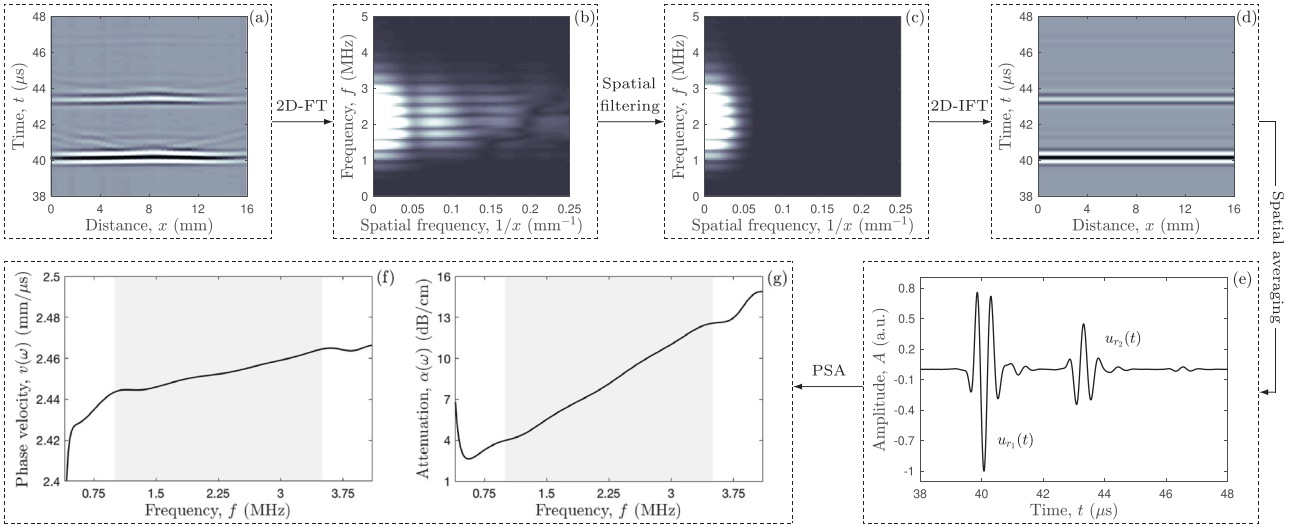

FIG. 5. (Color online) Flowchart of the dedicated signal processing steps, which are illustrated on the measurement performed on the stiffest homogeneous sample (i.e., $V_f = 0\%$): (a) Raw spatiotemporal signals; (b) 2D-FT of the recorded signals; (c) Resulting spectrum in the Fourier plane after applying a spatial low-pass filtering; (d) Retrieved spatiotemporal signals after applying a 2D-IFT; (e) Processed measurement after spatial averaging; and (f)–(g) Frequency-dependent phase velocity and attenuation obtained after applying a phase spectrum approach (PSA).

phase spectra. This was achieved by applying a two-dimensional Fourier transform (2D-FT) to the recorded spatiotemporal signals [see Fig. 5(b)]. Then, at each frequency f, a low-pass finite impulse response filter was applied to the resulting signals in the Fourier plane [see Fig. 5(c)]. Finally, the plane wavefronts were recovered in the time-domain by applying a 2D inverse Fourier transform (IFT) to the filtered spectra [see Fig. 5(d)]. The signals obtained on each element were then averaged [see Fig. 5(e)]. As can be observed, the resulting reflected signal $u_r(t)$ is generally compound of at least two echoes corresponding to reflections from the front and back faces of the sample, denoted by $u_{r_1}(t)$ and $u_{r_2}(t)$. A second step consisted in applying a phase spectrum approach (PSA) to these two reflected echoes, in order to retrieve the frequency-dependent phase velocity and attenuation of the sample. The frequency-dependent phase velocity $v(\omega)$ was derived as in He and Zheng (2001) and Raišutis *et al.* (2007),

$$v(\omega) = \frac{2D}{\Delta t + \Delta\phi/\omega}, \tag{18}$$

where D is the sample thickness, $\Delta\phi$ is the phase spectra difference between the two reflected echoes, and $\Delta t = t_2 - t_1$ is the time delay between the two reflected echoes, which was determined using the cross correlation of $u_{r_1}(t)$ and $-u_{r_2}(t)$ [recall Fig. 5(e)].

In the same way, the frequency-dependent attenuation $\alpha(\omega)$ was calculated as

$$\alpha(\omega) = \frac{1}{2D}\ln\left(\left|\frac{A_1(\omega)T(\omega)}{A_2(\omega)}\right|\right), \tag{19}$$

where $A_1(\omega)$ and $A_2(\omega)$ are the amplitude spectra of the two reflected echoes and $T(\omega)$ is the power transmission coefficient, which is defined as

$$T(\omega) = \frac{4Z_wZ_s(\omega)}{(Z_w + Z_s(\omega))^2}, \tag{20}$$

where $Z_w = \rho_w c_w$ and $Z_s(\omega) = \rho_s v(\omega)$ are the acoustic impedances of water and the sample, respectively, with ρ_w and ρ_s being their respective mass densities. The latter was determined based on a simple mixing rule,

$$\rho_s(V_f) = \rho_{\mathrm{TB}^+} \cdot V_f + \rho_{\mathrm{VW}^+} \cdot (1 - V_f), \tag{21}$$

where $\rho_{\mathrm{TB}^+} = 1.143$ g.cm^{-3} and $\rho_{\mathrm{VW}^+} = 1.177$ g.cm^{-3} were measured using a micrometer for the volume and a high accuracy balance for the mass. The sound speed in water, c_w, was set according to the water tank temperature (Marczak, 1997).

Figures 5(f)–5(g) depict the retrieved phase velocity $v(\omega)$ and attenuation $\alpha(\omega)$ for this sample. As can be observed, within the useful bandwidth (indicated as a gray area), the phase velocity $v(\omega)$ increases with frequency, thus indicating that the sample is slightly dispersive, whereas the attenuation $\alpha(\omega)$ increases nearly linearly as a function of the frequency.

These signal processing steps were applied to all homogeneous samples and the resulting evolution of the ultrasound characteristics as a function of the volume fraction V_f of TB$^+$ is depicted in Fig. 6 for three different frequencies. As expected, the phase velocity decreases with increasing V_f of TB$^+$, whereas the attenuation increases with increasing V_f of TB$^+$. It should be noted that both ultrasound characteristics can be remarkably explained by a linear approximation. These trends remain valid within the considered useful frequency bandwidth (data not shown).

B. Inverse problem

Altogether, our observations suggested that the experimental dispersion relation should yield a frequency-dependent phase velocity and a power-law attenuation, which *a posteriori* justified the model approximation presented in Sec. III A.

https://doi.org/10.1121/10.0009630

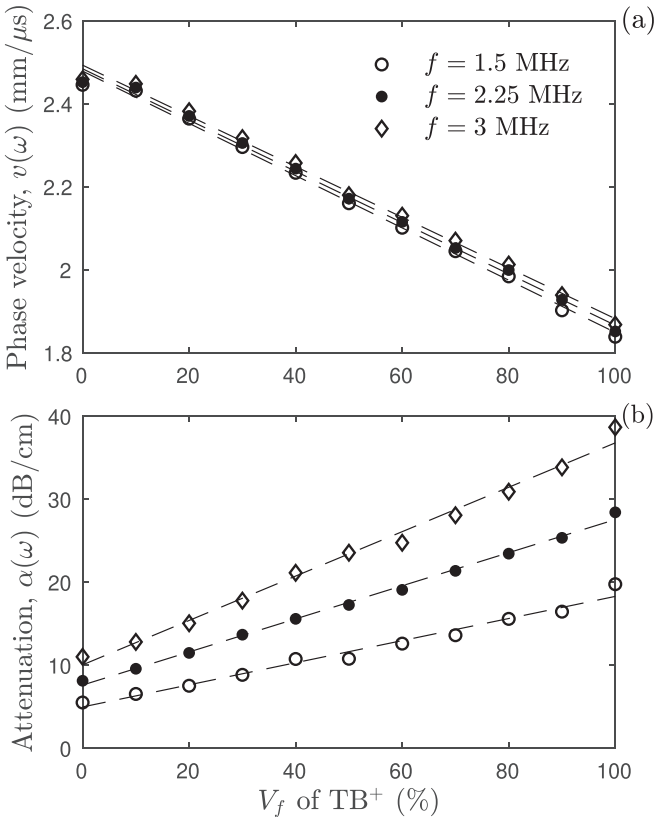

FIG. 6. Evolution of the (a) phase velocity $v(\omega)$ and (b) attenuation $\alpha(\omega)$ as a function of the volume fraction V_f of TB$^+$ for three different frequencies f. Linear fits are plotted in dashed lines for comparison.

To further investigate the ability of this model to predict experimentally observed data, we proposed an optimization procedure to identify the model parameters $\boldsymbol{\theta} = [v_1\ \alpha_0\ r]$ that minimize the following objective function $F(\boldsymbol{\theta})$ in a least squares sense as

$$F(\boldsymbol{\theta}) = \sqrt{\frac{1}{N}\sum_{n=1}^{N}\left|\frac{k(\omega_n) - k(\omega_n;\boldsymbol{\theta})}{k(\omega_n)}\right|^2}, \tag{22}$$

where $k(\omega_n)$ and $k(\omega_n;\boldsymbol{\theta})$ denote the measured and modeled complex wavenumbers at the n-th frequency, respectively, while N is the length of the useful frequency bandwidth on which the optimization is performed [recall the gray area in Figs. 5(f)–5(g)]. As the measurement of the attenuation $\alpha(\omega)$ evidenced that most samples follow a power-law with an exponent r close to 1, we hypothesized that its value was constant for all homogeneous samples. Therefore, the minimization was performed by sweeping r from 1 to 1.5 with a step of 0.01. For each r, the minimization of $[v_1\ \alpha_0]$ was achieved with a gradient-based method using the built-in sequential quadratic programming algorithm for constrained nonlinear optimization from Matlab (The MathWorks Inc., Natick, MA). Formally, the optimal model parameters result from

$$\hat{\boldsymbol{\theta}} = \arg\min_{r}\left(\frac{1}{N_r}\sum_{i=1}^{N_r}\left(\arg\min_{v_1,\alpha_0,r_i} F_i(\boldsymbol{\theta})\right)\right), \tag{23}$$

where N_r is the number of tested values for the power-law exponent r. To serve as an example, Fig. 7 depicts the optimal matching between the measured and modeled phase velocity and attenuation for the homogeneous samples with a volume fraction V_f of TB$^+$ equal to 30%, 50%, and 70%, which shows an excellent agreement on the useful frequency bandwidth. For these cases, the identified model parameters were $v_1 = [2.13\ \ 1.97\ \ 1.84]$ mm/μs, $\alpha_0 = [0.59\ \ 0.76\ \ 0.94]$ dB/cm/(rad.MHz)^r, and $r = 1.17$.

This minimization procedure was then applied to all homogeneous samples, in order to assess the relationship between the volume fraction and the optimal model parameters. Figure 8 depicts the evolution of the optimal mechanical

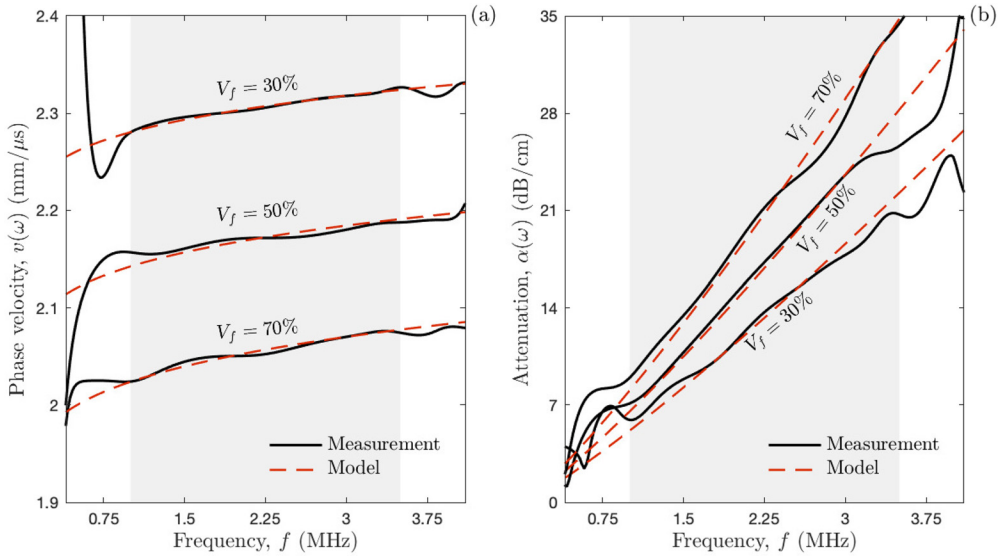

FIG. 7. (Color online) Optimal matching between the measured and modeled (a) phase velocity and (b) attenuation, for the homogeneous samples with a volume fraction V_f of TB$^+$ equal to 30%, 50%, and 70%. The gray area shows the useful frequency bandwidth on which the inversion process was performed.

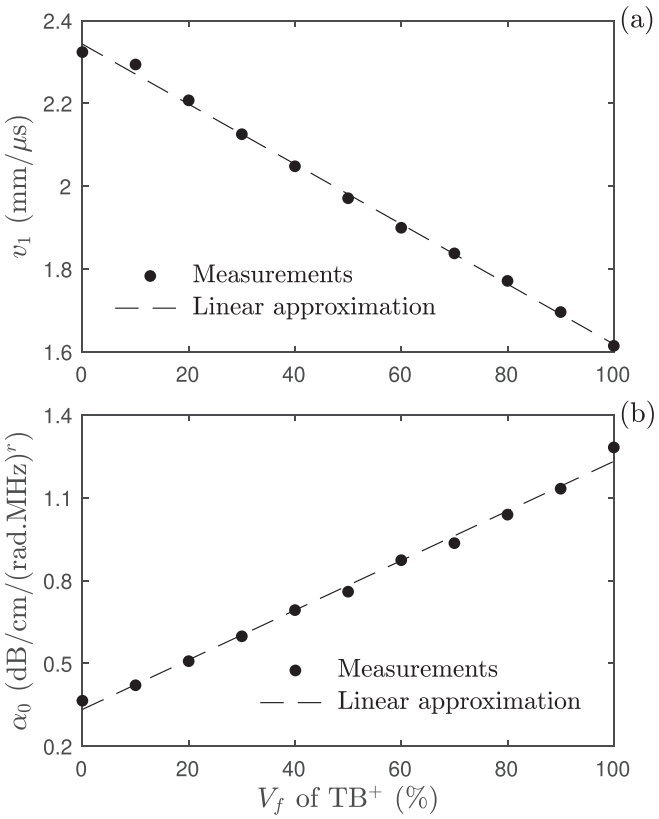

FIG. 8. Evolution of the optimal model parameters $\boldsymbol{\theta}$, i.e., (a) v_1 and (b) α_0 ($r = 1.17$), as a function of the volume fraction V_f of TB$^+$.

characteristics v_1 and α_0 as a function of the volume fraction V_f of TB$^+$. As can be observed, both mechanical characteristics are remarkably approximated by a linear regression analysis ($R^2 = 0.99$, $p < 0.05$), with root mean square errors for v_1 and α_0 that are equal to 0.01 mm/μs and 0.02 dB/cm/(rad.MHz)^r, respectively. The resulting linear relationships are

$$\begin{aligned} v_1(V_f) &= -0.725 \cdot V_f + 2.343, \\ \alpha_0(V_f) &= 0.899 \cdot V_f + 0.333, \end{aligned} \tag{24}$$

for a constant exponent $r = 1.17$.

V. MODEL VALIDATION

The goal of this section was to compare the measurements performed on the heterogeneous samples with those predicted by the mechanical model presented in Sec. III B. Towards this goal, the signals were directly compared in the time-domain. Therefore, the signal processing steps (a)–(e) were applied to the measured signals (recall Fig. 5). On the other hand, for each configuration depicted in Fig. 2, the relationships [Eqs. (21) and (24)] were used to feed the model and subsequently solve Eq. (17).

Figure 9 depicts the measured (continuous black line) and modeled (dashed red line) signals for the six heterogeneous samples with different graded profiles. As can be observed, these signals consist of two main invariant echoes, which correspond to reflections from the front and back faces of the samples (depicted by green arrows), respectively. The signal fluctuations in-between represent a signature of the reflections from the interphase (depicted by blue arrows), which differ in time of arrival and amplitude across the different samples, thus indicating that the proposed measurement technique is sensitive to different functionally graded profiles. As expected, the two reference profiles highlighting a discontinuous transition [see Figs. 9(a)–9(b)] present stronger reflections in the form of a single echo and two superimposed echoes, which are due to the presence of a sharp interface and a homogeneous interphase, respectively. In contrast, for the two profiles displaying a continuous transition [see Figs. 9(c)–9(d)], the reflections are nearly completely filtered out. It can be noted that for the smoothly varying profile, the remaining signal consists of lower frequency components than for the linearly varying one (evidenced by the space between the multiple headed arrow). Interestingly, for the two damaged profiles [see Figs. 9(e)–9(f)], the local and sudden drop in volume fraction induces a local decrease in the mechanical characteristics as well, which lead to the presence of higher amplitude fluctuations than for their undamaged counterparts.

Overall, there is an excellent agreement between the model and the measurements, thus confirming the choice of a modeling approach that incorporates a frequency-dependent phase velocity and a power-law attenuation. Although the measurements alone could allow discriminating different graded profiles to some extent [e.g., Figs. 9(a)–9(d)], our model-based approach allows quantifying finely-tuned differences in the manufacturing process [e.g., Figs. 9(e)–9(f)]. Therefore, such a model could be further used as a guide towards the design of specific configurations.

VI. DISCUSSION

In this study, we proposed a nondestructive method for the characterization of bioinspired functionally graded soft-to-hard composites by ultrasound. These were designed and additively manufactured using a voxel-by-voxel multi-material 3D printing technique, which allowed for a local and accurate control of the spatial arrangement of two phases with highly dissimilar properties (i.e., a rigid glassy polymer and an elastomeric polymer). Both homogeneous and heterogeneous samples with functional grading were obtained by adjusting the relative proportions of these two photopolymers. All samples were then measured in the MHz-regime using a multielement probe driven by a multichannel electronics. In a first part, the signals retrieved from the homogeneous samples were processed using a spectral method to extract information about the phase velocity and attenuation dispersion. From these acoustic characteristics, relationships between the model parameters and the material composition were identified by solving a model-based inverse problem. In a second part, these relationships were used to feed a multilayered model based on the transfer matrix formalism, which could be validated by systematically comparing the predicted signals to those measured on the heterogeneous samples with functional grading.

https://doi.org/10.1121/10.0009630

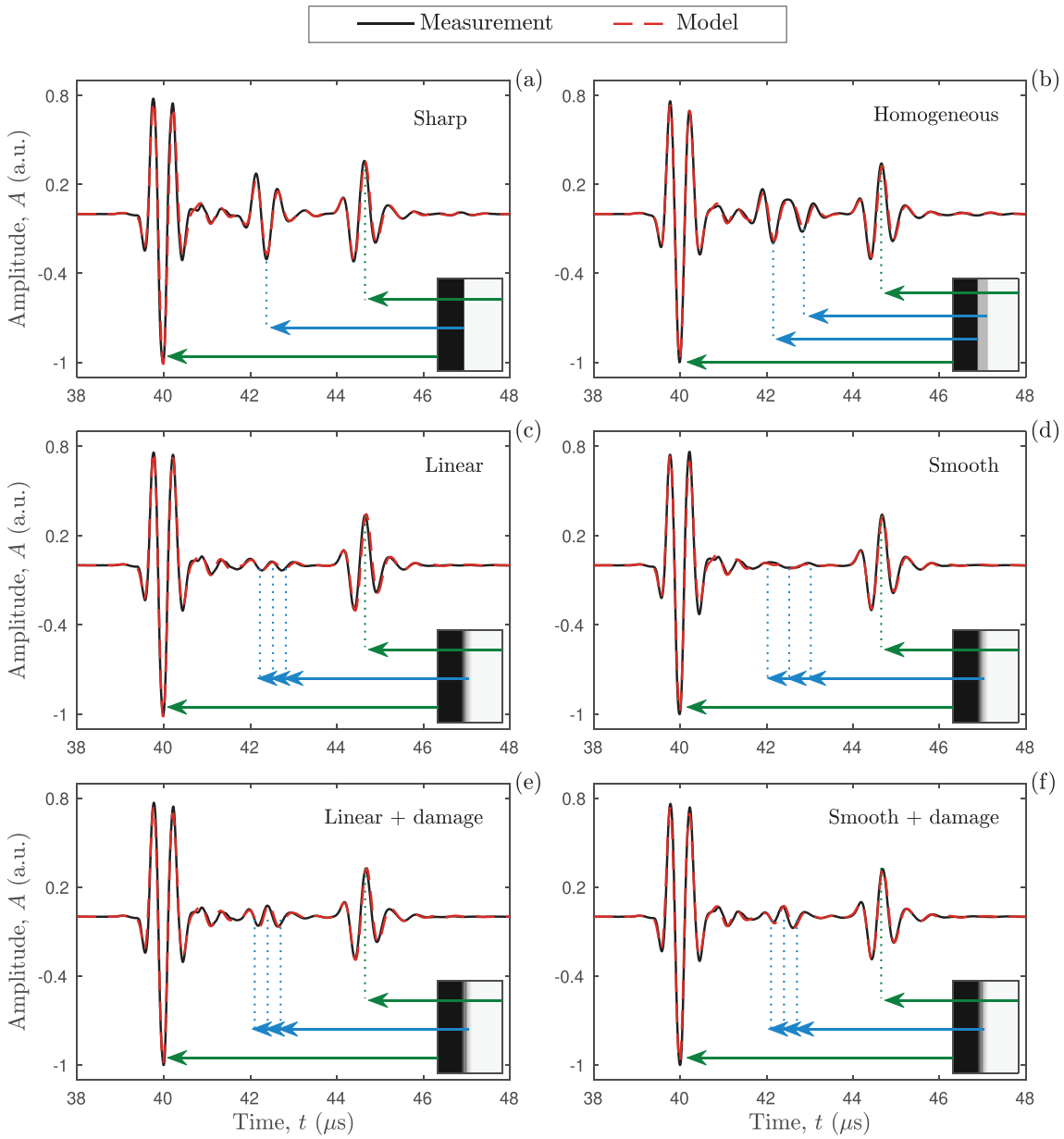

FIG. 9. (Color online) Comparison between the measurement and the model for the six heterogeneous samples (recall Fig. 2): (a) Bilayer sample with a sharp transition, (b) trilayer sample with a homogeneous interphase, (c) sample with a linearly varying interphase, (d) sample with a smoothly varying interphase, (e) sample with a localized damage across the linearly varying interphase, and (f) sample with a localized damage across the smoothly varying interphase. The inserts schematize the different arrivals of the signal components reflected from the front and back faces of the immersed sample, as well as from the interphase.

The main findings were as follows: First, for the considered photopolymers, the measurements performed on the macroscopically homogeneous samples evidenced that the dispersion relation exhibited a frequency-dependent phase velocity and a power-law attenuation. Such behavior could be adequately modeled using the Szabo wave equation. Second, the derived relationships between the mechanical characteristics (i.e., v_1 and α_0) and the composition (i.e., volume fraction of the compliant polymer) were shown to be linear. It should be noted that this is not necessarily the case for the elastic modulus and strength, which were shown to follow a nonlinear trend with the volume fraction (Slesarenko and Rudykh, 2018; Zorzetto *et al.*, 2020). Third, although the 3D printing process, which delivers complex patterns at the microscale, yields a rather continuous functional grading at the macroscale, the heterogeneous samples could be satisfactorily modeled as successive piecewise homogeneous layers. Fourth, the proposed model allowed discriminating different profiles displaying slight variations of the material and mechanistic ingredients.

For the homogeneous samples, a direct quantitative comparison with earlier reported acoustic characteristics is difficult. Indeed, the applied ultrasonic measurement technique, in particular the explored frequency regime, along with the investigated samples generally differ from one study to another. For instance, by performing through-transmission measurements on a 3 mm-thick sample using contact longitudinal transducers at 1 MHz, Livings *et al.* (2015) reported a

value of 2.46 mm/μs for the phase velocity of VW^+. By carrying out pulse-echo measurements on a water-immersed 0.5 mm-thick sample using a focused single-element transducer in the frequency range of 15–30 MHz, Jacquet *et al.* (2015) reported values of 2.63 mm/μs and 110 dB/cm for the frequency-dependent phase velocity and attenuation of VW^+ evaluated at 20 MHz, respectively. In another related study, by performing through-transmission measurements on 16 μm-thick samples using air-coupled transducers in the frequency range of 0.15–0.35 MHz, Fariñas *et al.* (2016) reported values of 1.9 and 2.8 MRayl for the acoustic impedances of TB^+ and VW^+, respectively. In a recent study closely related to ours, by carrying out transmission measurements on a water-immersed 4 mm-thick sample using a focused single-element transducer in the frequency range of 1–3.5 MHz, Bakaric *et al.* (2021) reported values of around 2.50 mm/μs and 9 dB/cm for the frequency-dependent phase velocity and attenuation of VW+, respectively. Extrapolating our modeling results to these frequencies yield (1) values of 2.43, 2.45, and 2.52 mm/μs for the phase velocity of VW^+ at 1, 2.25, and 20 MHz, respectively; (2) values of 8.1 and 104 dB/cm for the attenuation of VW^+ at 2.25 and 20 MHz, respectively; and (3) values of 2.02 and 2.84 MRayl for the acoustic impedances of TB^+ and VW^+ at 0.25 MHz, respectively. These are all in excellent agreement with the reported literature values, thus indicating that our modeling assumptions are reasonable for a wide frequency band. No comparison could be performed for the heterogeneous samples with functional grading and programmed damage as, to the authors' best knowledge, there are no studies in the open literature reporting such measurements. Nevertheless, the excellent agreement between the measured and modeled signals reported in Fig. 9 allow us to be confident in the proposed formalism.

Despite these promising results, several simplifications were adopted at different stages of the proposed methods: First, the dispersive loss was modeled here by introducing a fractional derivative into the wave equation. Although such a phenomenological approach allowed modeling the observed frequency-dependent phase velocity and power-law attenuation in a suitable way, it prevents a proper identification of the underlying loss mechanisms. To this end, other routes could have been explored, such as the combination of hard and soft modeling (Martinsson *et al.*, 2008), the incorporation of a continuum of relaxation mechanisms (Näsholm and Holm, 2011), or the formulation of a constitutive equation within the strain-gradient framework (Rosi *et al.*, 2018). Second, it should be noted that we only solved the forward problem for the heterogeneous samples by modeling the wave-interphase interactions based on the knowledge of the mechanical properties of the individual constituents. A challenging but necessary step towards the evaluation of such composites would be to solve the inverse problem (Bochud *et al.*, 2017), i.e., reconstructing the shape of the graded profile or identifying the damage location from the measured signals. Third, both sets of samples were characterized in normal incidence, thus delivering mechanical characteristics that are related to compression waves only. However, it is expected that shear waves may carry valuable information as well both for (i) recovering the engineering moduli (e.g., Young's modulus and Poisson's ratio) of the homogeneous samples under the assumption of mechanical isotropy, and (ii) studying the impact of damage mechanisms across the interphase on the reflected signals. A last concern is related to the replicated bioinspired feature, which was limited to a functional grading of properties along the z-direction. The latter is not the only feature that contribute to the mechanical effectiveness of the tendon-to-bone attachment. Indeed, the interdigitation at the interphase between tendon and bone, described as a wavelike structure, was shown to allow a gain in toughness, as well as a better distribution of the mechanical stresses on the fraction of tissue implied in this mechanism (Hu *et al.*, 2015).

Altogether, these limitations make the ultrasound characterization of bioinspired functionally graded soft-to-hard composites a challenging problem with much potential for future works. As a next step, we will adapt our experimental setup to the double through-transmission method in oblique incidence (Rokhlin and Wang, 1992), which allows for measurement of the phase velocity and attenuation of both longitudinal and shear waves. Future studies are also warranted to incorporate more complex mechanisms (e.g., porosity, anisotropy, and interphase roughness) in the 3D-printing and modeling processes. Overall, this research will not only be valuable for manufacturing and characterizing graded soft-to-hard composites inspired by the tendon-to-bone attachment, but also multi-material lattices and brick-and-mortar arrangements (Mirzaali *et al.*, 2020b), which can be found for instance at the bone-implant interphase (Hériveaux *et al.*, 2018) or the dentine-enamel connection in teeth (Messineo *et al.*, 2013). Given that 3D printing is experiencing a wide dissemination, our approach should be considered as a rapid, accurate and inexpensive quality inspection technique.

ACKNOWLEDGMENTS

The authors are in debt to Max Gattin for the fruitful discussions regarding the processing of the ultrasound signals and the Szabo wave equation. This work was partially supported by the BEST-AMUS project (IIN program, CNRS-INSIS, France).

[1]See supplementary material at https://www.scitation.org/doi/suppl/10.1121/10.0009630 for tables summarizing the dimensions and specificities of the two sets of 3D-printed samples.

Aghaei, A., Bochud, N., Rosi, G., and Naili, S. (**2021**). "Assessing the effective elastic properties of the tendon-to-bone insertion: A multiscale modeling approach," Biomech. Model Mechanobiol. **20**(2), 433–448.

Bakaric, M., Miloro, P., Javaherian, A., Cox, B. T., Treeby, B. E., and Brown, M. D. (**2021**). "Measurement of the ultrasound attenuation and dispersion in 3D-printed photopolymer materials from 1 to 3.5 MHz," J. Acoust. Soc. Am. **150**(4), 2798–2805.

Benjamin, M., Toumi, H., Suzuki, D., Redman, S., Emery, P., and McGonagle, D. (**2007**). "Microdamage and altered vascularity at the enthesis–bone interface provides an anatomic explanation for bone involvement in the Hla–B27–associated spondylarthritides and allied disorders," Arthritis Rheum. **56**(1), 224–233.

Bochud, N., Gomez, A., Rus, G., and Peinado, A. (**2015**). "A sparse digital signal model for ultrasonic nondestructive evaluation of layered materials," Ultrasonics **62**, 160–173.
Bochud, N., Laurent, J., Bruno, F., Royer, D., and Prada, C. (**2018**). "Towards real-time assessment of anisotropic plate properties using elastic guided waves," J. Acoust. Soc. Am. **143**(2), 1138–1147.
Bochud, N., Vallet, Q., Minonzio, J.-G., and Laugier, P. (**2017**). "Predicting bone strength with ultrasonic guided waves," Sci. Rep. **7**, 43628.
Cretu, N., and Nita, G. (**2004**). "Pulse propagation in finite elastic inhomogeneous media," Comput. Mater. Sci. **31**(3-4), 329–336.
Deymier, A. C., Schwartz, A. G., Cai, Z., Daulton, T. L., Pasteris, J. D., Genin, G. M., and Thomopoulos, S. (**2019**). "The multiscale structural and mechanical effects of mouse supraspinatus muscle unloading on the mature enthesis," Acta. Biomater. **83**, 302–313.
Dunlop, J. W. C., Weinkamer, R., and Fratzl, P. (**2011**). "Artful interfaces within biological materials," Mater. Today **14**(3), 70–78.
Fariñas, M. D., Álvarez-Arenas, T., Cummins, G., Desmulliez, M. P. Y., Seetohul, V., and Cochran, S. (**2016**). "Assessment of the ultrasonic properties of additive manufactured materials for passive components of piezoelectric transducers," in *IEEE International Ultrasonics Symposium*, September 18–21, Tours, France, pp. 1–4.
Foster, D., Dapino, M., and Babu, S. (**2013**). "Elastic constants of ultrasonic additive manufactured al 3003-h18," Ultrasonics **53**(1), 211–218.
Giannatsis, J., and Dedoussis, V. (**2009**). "Additive fabrication technologies applied to medicine and health care: A review," Int. J. Adv. Manuf. Syst. **40**(1–2), 116–127.
He, P., and Zheng, J. (**2001**). "Acoustic dispersion and attenuation measurement using both transmitted and reflected pulses," Ultrasonics **39**(1), 27–32.
Hériveaux, Y., Nguyen, V.-H., and Haïat, G. (**2018**). "Reflection of an ultrasonic wave on the bone-implant interface: A numerical study of the effect of the multiscale roughness," J. Acoust. Soc. Am. **144**(1), 488–499.
Honarvar, F., and Varvani-Farahani, A. (**2020**). "A review of ultrasonic testing applications in additive manufacturing: Defect evaluation, material characterization, and process control," Ultrasonics **108**, 106227.
Hu, Y., Birman, V., Deymier-Black, A., Schwartz, A. G., Thomopoulos, S., and Genin, G. M. (**2015**). "Stochastic interdigitation as a toughening mechanism at the interface between tendon and bone," Biophys. J. **108**(2), 431–437.
Jacquet, J.-R., Levassort, F., Ossant, F., and Grégoire, J.-M. (**2015**). "3D printed phantom for high frequency ultrasound imaging," in *IEEE International Ultrasonics Symposium*, October 21–24, Taipei, Taiwan, pp. 1–4.
Javidrad, H., and Salemi, S. (**2020**). "Determination of elastic constants of additive manufactured inconel 625 specimens using an ultrasonic technique," Int. J. Adv. Manuf. Technol. **107**(11), 4597–4607.
Jia, Z., Yu, Y., Hou, S., and Wang, L. (**2019**). "Biomimetic architected materials with improved dynamic performance," J. Mech. Phys. Solids **125**, 178–197.
Kelly, J. F., McGough, R. J., and Meerschaert, M. M. (**2008**). "Analytical time-domain Green's functions for power-law media," J. Acoust. Soc. Am. **124**(5), 2861–2872.
Leleux, A., Micheau, P., and Castaings, M. (**2013**). "Long range detection of defects in composite plates using lamb waves generated and detected by ultrasonic phased array probes," J. Nondestruct. Eval. **32**(2), 200–214.
Libonati, F., Gu, G. X., Qin, Z., Vergani, L., and Buehler, M. J. (**2016**). "Bone-inspired materials by design: Toughness amplification observed using 3D printing and testing," Adv. Eng. Mater. **18**(8), 1354–1363.
Liu, Y., Thomopoulos, S., Chen, C., Birman, V., Buehler, M. J., and Genin, G. M. (**2014**). "Modelling the mechanics of partially mineralized collagen fibrils, fibres and tissue," J. R. Soc. Interface **11**(92), 20130835.
Liu, Z., Meyers, M. A., Zhang, Z., and Ritchie, R. O. (**2017**). "Functional gradients and heterogeneities in biological materials: Design principles, functions, and bioinspired applications," Prog. Mater. Sci. **88**, 467–498.
Livings, R., Dayal, V., and Barnard, D. (**2015**). "Characterization of 3D rapid prototyped polymeric material by ultrasonic methods," AIP Conf. Proc. **1650**, 807–816.
Marczak, W. (**1997**). "Water as a standard in the measurements of speed of sound in liquids," J. Acoust. Soc. Am. **102**(5), 2776–2779.
Martinsson, J., Hägglund, F., and Carlson, J. E. (**2008**). "Complete post-separation of overlapping ultrasonic signals by combining hard and soft modeling," Ultrasonics **48**(5), 427–443.
Meisel, N. A., Dillard, D. A., and Williams, C. B. (**2018**). "Impact of material concentration and distribution on composite parts manufactured via multi-material jetting," Rapid Prototyp. J. **24**(5), 872–879.
Messineo, M. G., Frontini, G. L., Eliçabe, G. E., and Gaete-Garretón, L. (**2013**). "Equivalent ultrasonic impedance in multilayer media. A parameter estimation problem," Inverse Probl. Sci. Eng. **21**(8), 1268–1287.
Mirzaali, M., de la Nava, A. H., Gunashekar, D., Nouri-Goushki, M., Veeger, R., Grossman, Q., Angeloni, L., Ghatkesar, M., Fratila-Apachitei, L., Ruffoni, D., Doubrovskid, E. L., and Zadpoora, A. A. (**2020a**). "Mechanics of bioinspired functionally graded soft-hard composites made by multi-material 3D printing," Compos. Struct. **237**, 111867.
Mirzaali, M. J., Cruz Saldívar, M., Herranz de la Nava, A., Gunashekar, D., Nouri-Goushki, M., Doubrovski, E. L., and Zadpoor, A. A. (**2020b**). "Multi-material 3D printing of functionally graded hierarchical soft–hard composites," Adv. Eng. Mater. **22**(7), 1901142.
Näsholm, S. P., and Holm, S. (**2011**). "Linking multiple relaxation, power-law attenuation, and fractional wave equations," J. Acoust. Soc. Am. **130**(5), 3038–3045.
Perikamana, S. K. M., Lee, J., Ahmad, T., Kim, E. M., Byun, H., Lee, S., and Shin, H. (**2018**). "Harnessing biochemical and structural cues for tenogenic differentiation of adipose derived stem cells (ADSCs) and development of an *in vitro* tissue interface mimicking tendon-bone insertion graft," Biomaterials **165**, 79–93.
Rafiee, M., Farahani, R. D., and Therriault, D. (**2020**). "Multi-material 3D and 4D printing: A survey," Adv. Sci. **7**(12), 1902307.
Raišutis, R., Kažys, R., and Mažeika, L. (**2007**). "Application of the ultrasonic characterization methods for highly attenuating plastic materials," NDT E Int. **40**(4), 324–332.
Rokhlin, S. I., and Wang, W. (**1992**). "Double through-transmission bulk wave method for ultrasonic phase velocity measurement and determination of elastic constants of composite materials," J. Acoust. Soc. Am. **91**(6), 3303–3312.
Rosi, G., Placidi, L., and Auffray, N. (**2018**). "On the validity range of strain-gradient elasticity: A mixed static-dynamic identification procedure," Eur. J. Mech. A Solids **69**, 179–191.
Rubio, W. M., Paulino, G. H., and Silva, E. C. N. (**2012**). "Analysis, manufacture and characterization of Ni/Cu functionally graded structures," Mater. Des. **41**, 255–265.
Saadat, F., Deymier, A., Birman, V., Thomopoulos, S., and Genin, G. (**2016**). "The concentration of stress at the rotator cuff tendon-to-bone attachment site is conserved across species," J. Mech. Behav. Biomed. Mater. **62**, 24–32.
Sasso, M., Haïat, G., Yamato, Y., Naili, S., and Matsukawa, M. (**2007**). "Frequency dependence of ultrasonic attenuation in bovine cortical bone: An *in vitro* study," Ultrasound Med. Biol. **33**(12), 1933–1942.
Slesarenko, V., and Rudykh, S. (**2018**). "Towards mechanical characterization of soft digital materials for multimaterial 3D-printing," Int. J. Eng. Sci. **123**, 62–72.
Slotwinski, J. A., Garboczi, E. J., and Hebenstreit, K. M. (**2014**). "Porosity measurements and analysis for metal additive manufacturing process control," J. Res. Nat. Inst. Stand. Technol. **119**, 494–528.
Studart, A. R. (**2016**). "Additive manufacturing of biologically-inspired materials," Chem. Soc. Rev. **45**(2), 359–376.
Szabo, T. L., and Wu, J. (**2000**). "A model for longitudinal and shear wave propagation in viscoelastic media," J. Acoust. Soc. Am. **107**(5), 2437–2446.
Tits, A., and Ruffoni, D. (**2020**). "Joining soft tissues to bone: Insights from modeling and simulations," Bone Rep. **14**, 100742.
Velasco-Hogan, A., Xu, J., and Meyers, M. A. (**2018**). "Additive manufacturing as a method to design and optimize bioinspired structures," Adv. Mater. **30**(52), 1800940.
Zorzetto, L., Andena, L., Briatico-Vangosa, F., De Noni, L., Thomassin, J.-M., Jérôme, C., Grossman, Q., Mertens, A., Weinkamer, R., Rink, M., and Ruffoni, D. (**2020**). "Properties and role of interfaces in multimaterial 3D printed composites," Sci. Rep. **10**(1), 22285.
Zorzetto, L., and Ruffoni, D. (**2019**). "Wood-inspired 3D-printed helical composites with tunable and enhanced mechanical performance," Adv. Funct. Mater. **29**(1), 1805888.